ENVIRONMENTAL SCIENCE

Australian shelf sediments reveal shifts in Miocene Southern Hemisphere westerlies

Jeroen Groeneveld,[1]* Jorijntje Henderiks,[2] Willem Renema,[3] Cecilia M. McHugh,[4] David De Vleeschouwer,[1] Beth A. Christensen,[5] Craig S. Fulthorpe,[6] Lars Reuning,[7] Stephen J. Gallagher,[8] Kara Bogus,[9] Gerald Auer,[10†] Takeshige Ishiwa,[11] Expedition 356 Scientists[‡]

Global climate underwent a major reorganization when the Antarctic ice sheet expanded ~14 million years ago (Ma) (*1*). This event affected global atmospheric circulation, including the strength and position of the westerlies and the Intertropical Convergence Zone (ITCZ), and, therefore, precipitation patterns (*2*–*5*). We present new shallow-marine sediment records from the continental shelf of Australia (International Ocean Discovery Program Sites U1459 and U1464) providing the first empirical evidence linking high-latitude cooling around Antarctica to climate change in the (sub)tropics during the Miocene. We show that Western Australia was arid during most of the Middle Miocene. Southwest Australia became wetter during the Late Miocene, creating a climate gradient with the arid interior, whereas northwest Australia remained arid throughout. Precipitation and river runoff in southwest Australia gradually increased from 12 to 8 Ma, which we relate to a northward migration or intensification of the westerlies possibly due to increased sea ice in the Southern Ocean (*5*). Abrupt aridification indicates that the westerlies shifted back to a position south of Australia after 8 Ma. Our midlatitude Southern Hemisphere data are consistent with the inference that expansion of sea ice around Antarctica resulted in a northward movement of the westerlies. In turn, this may have pushed tropical atmospheric circulation and the ITCZ northward, shifting the main precipitation belt over large parts of Southeast Asia (*4*).

INTRODUCTION

The midlatitude westerlies, located between Australia and Antarctica (Fig. 1), are part of the Southern Annular Mode (SAM). The SAM can be defined as the zonal mean atmospheric pressure difference between the midlatitudes and Antarctica (*6*). Increases in this atmospheric pressure contrast result in a strengthening and northward migration of the Southern Hemisphere westerlies (*6*, *7*). Accordingly, westerly fronts bring precipitation to southwest Australia during austral winter. The position of the westerlies is also influenced by sea surface temperatures (SSTs) and the extent of sea ice around Antarctica (*8*). The increase in Antarctic sea ice cover during austral winter pushes the westerlies and consequently the Hadley cell northward, intensifying atmospheric circulation over Australia (*2*, *9*–*11*). The Southern Hemisphere Hadley circulation connects the dry descending air of the subtropical ridge with low-latitude moisture and the rising air of the Intertropical Convergence Zone (ITCZ) (Fig. 2) (*9*). The seasonal movement of the ITCZ controls the summer and winter monsoons over Southeast Asia and Australia. In recent decades, changes in the SAM have led to a drying in southwest Australia (*6*), but it remains unclear how this climate response is expressed on longer, million-year time scales.

The continental shelf of Western Australia lies directly adjacent to today's semi-arid continent and hosts a barely explored archive of Neogene climate variability. The International Ocean Discovery Program (IODP) Expedition 356 recently recovered sediments that bring new insights about the Miocene history of aridity and humidity in Australia (*12*). The Miocene Australian continent was located 5° to 10° farther south than at present (*13*), so southwest Australia was under the direct influence of the westerlies (Fig. 2). The northward tectonic movement alone would have gradually shifted southwest Australia out of the influence of the westerlies and enhanced aridity, assuming weather systems remained the same. However, our data show an intensification of precipitation and fluvial runoff during this time, suggesting the influence of additional controls.

RESULTS

IODP Site U1459 in the Perth Basin and Site U1464 in the Roebuck Basin are the southernmost and northernmost sites drilled in a latitudinal transect (Fig. 1) (*12*). Nannofossil and benthic foraminiferal biostratigraphy constrain ages for both sites from earliest Middle [~16 to 18 Ma (million years ago)] to Late Miocene (5.59 Ma) (table S1, and figs. S1 and S2). Time series analysis of the downhole wireline logs documents an eccentricity-controlled signal, which supports the biostratigraphic age model, suggesting relatively constant sedimentation rates on million-year time scales (figs. S1 and S2). At the northern site (U1464), the sediments consist of shallow-marine and, possibly, subaerial deposits including tidally laminated sediments and evaporitic nodules, suggesting arid conditions (fig. S1). The most arid interval (~14.1 to 12.6 Ma) is represented by sabkha-like sediments including organic-rich and carbonate-poor layers (fig. S1). In contrast, sediments recovered at the southern site (U1459) are typified by grain-supported

[1]MARUM–Center for Marine and Environmental Sciences, Department of Geosciences, University of Bremen, 28359 Bremen, Germany. [2]Department of Earth Sciences, Uppsala University, Villavägen 16, 75236 Uppsala, Sweden. [3]Naturalis Biodiversity Center, PO Box 9517, 2300 RA Leiden, Netherlands. [4]School of Earth and Environmental Sciences, Queens College (City University of New York), 65-30 Kissena Boulevard, Flushing, NY 11367, USA. [5]Environmental Studies, Adelphi University, 1 South Avenue SCB 201, Garden City, NY 11530, USA. [6]Institute for Geophysics, University of Texas at Austin, 10100 Burnet Road (R2200), Austin, TX 78758–4445, USA. [7]Energy and Mineral Resources Group (EMR), Geological Institute Rheinisch-Westfälische Technische Hochschule (RWTH), Aachen University, Wuellnerstrasse, Aachen 52056, Germany. [8]School of Earth Sciences, University of Melbourne, Melbourne, Victoria 3010, Australia. [9]International Ocean Discovery Program, Texas A&M University, 1000 Discovery Drive, College Station, TX 77845–9547, USA. [10]Institute of Earth Sciences, University of Graz, Heinrichstrasse 26, Graz 8010, Austria. [11]Atmosphere and Ocean Research Institute, University of Tokyo, 5-1-5 Kashiwanoha, Kashiwa-shi, Chiba 277-8564, Japan.
*Corresponding author. Email: jgroeneveld@uni-bremen.de
†Present address: Department of Biogeochemistry, Japan Agency for Marine-Earth Science and Technology (JAMSTEC), 2-15 Natsushima-cho, Yokosuka, Kanagawa 237-0061, Japan.
‡See the Supplementary Materials for a complete list of Expedition 356 Scientists.

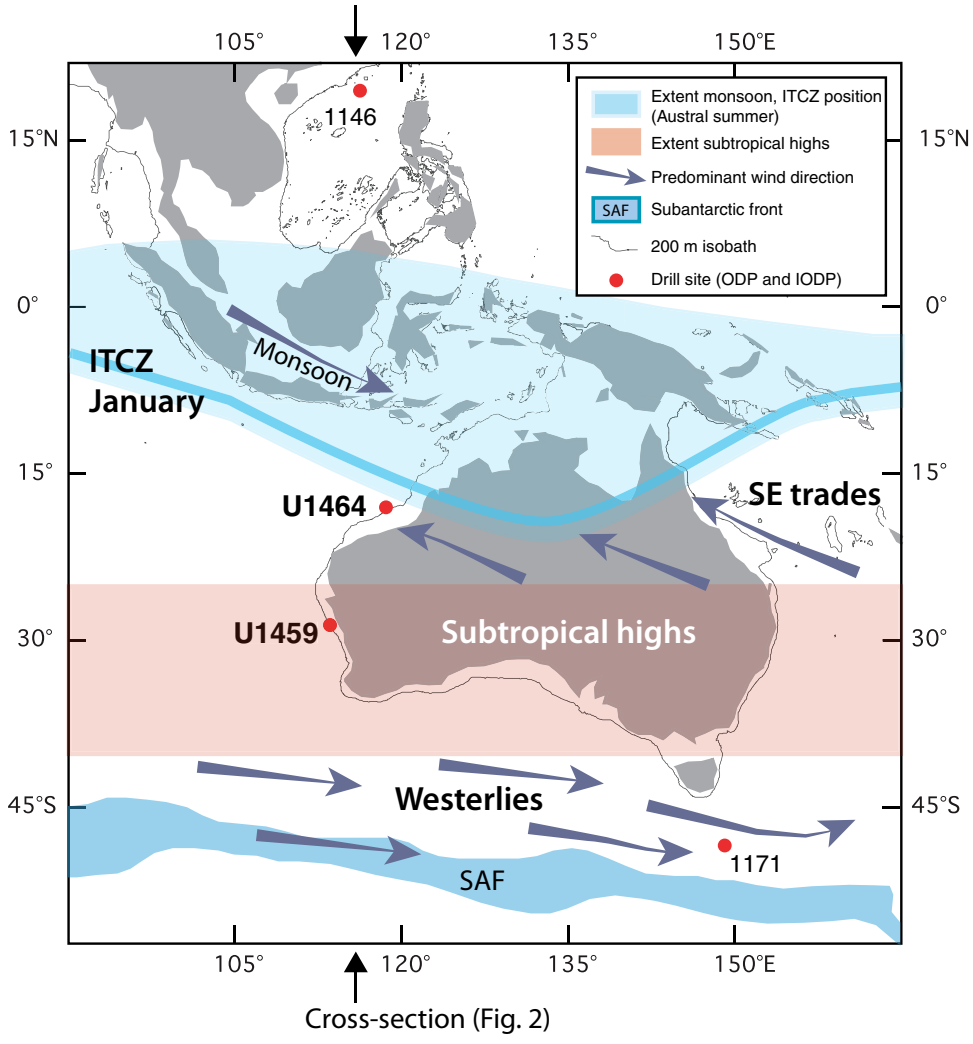

Fig. 1. Map of Australia and Southeast Asia showing site locations and prevailing atmospheric circulation features. Red dots indicate the study sites (IODP Sites U1459 and U1464) and sites used for interpretation from the South China Sea (ODP Site 1146) (*4*, *28*) and off Tasmania (ODP Site 1171) (*5*). Major weather features and prevailing wind directions are indicated, including ITCZ, the westerlies, and the Subantarctic Front (SAF).

dolomitic limestones with a few intervals of quartz-rich sandstones deposited in a shelf setting (>100-m water depth) influenced by river input (fig. S2).

Downhole wireline logs of potassium (K), thorium (Th), and their ratio Th/K at both carbonate-dominated sites provide a continuous record of the degree of siliciclastic, riverine input (Fig. 3). The K component of the gamma ray logs is often used to infer the concentration of K-bearing aluminosilicates, mainly clays and K feldspars (*14*). An increase in K has previously been interpreted as a relative increase in siliciclastic sediment supply via rivers, indicative of a change from drier to wetter conditions off the coast of Western Australia (*15*, *16*). X-ray diffraction (XRD) analyses to determine bulk mineralogy confirm that K feldspars are the main K-bearing minerals in the sediments of Site U1459 (fig. S3). Thorium not only occurs in aluminosilicates but also in heavy minerals, which are mainly wind-transported and thus related to more arid conditions. We therefore use the Th/K ratio to provide a dilution-independent record, supported by variations in the absolute K content (see Supplementary Text). The configuration of the paleodrainage systems in Australia during the Miocene was similar to today (*17*). Therefore, we assume that the pathways of sediment supply and their relationship to continental climate were also similar to modern conditions. Accordingly, we interpret high Th/K values (Fig. 3A) as indicative for dry conditions and high K values (Fig. 3B) as showing variations in riverine input and, thus, the amount of rainfall over southwest Australia. At Site U1459, highest Th/K accompanied by low K (%) occurred before 11 Ma with significant amplitude variability. After 11 Ma, a switch to generally low Th/K and increasing K (%) took place. Highest Th/K values at Site U1464 show that the northwest was primarily affected by arid conditions, whereas K values remain low throughout the studied time interval. These results indicate that river-influenced conditions were mainly found in southwest Australia (Fig. 3). This contrasts with indications for wet conditions and rainforests during the Middle Miocene not only in the southeast but also in Central and Western Australia (*18*). On the other hand, our findings agree with modeling studies, suggesting that the monsoon was no more intense than today (*19*). In addition, no unequivocal evidence for humid vegetation types exists for the interior for the Middle Miocene (*20*). Following the slightly wetter conditions in southwest Australia during the Middle Miocene, conditions became

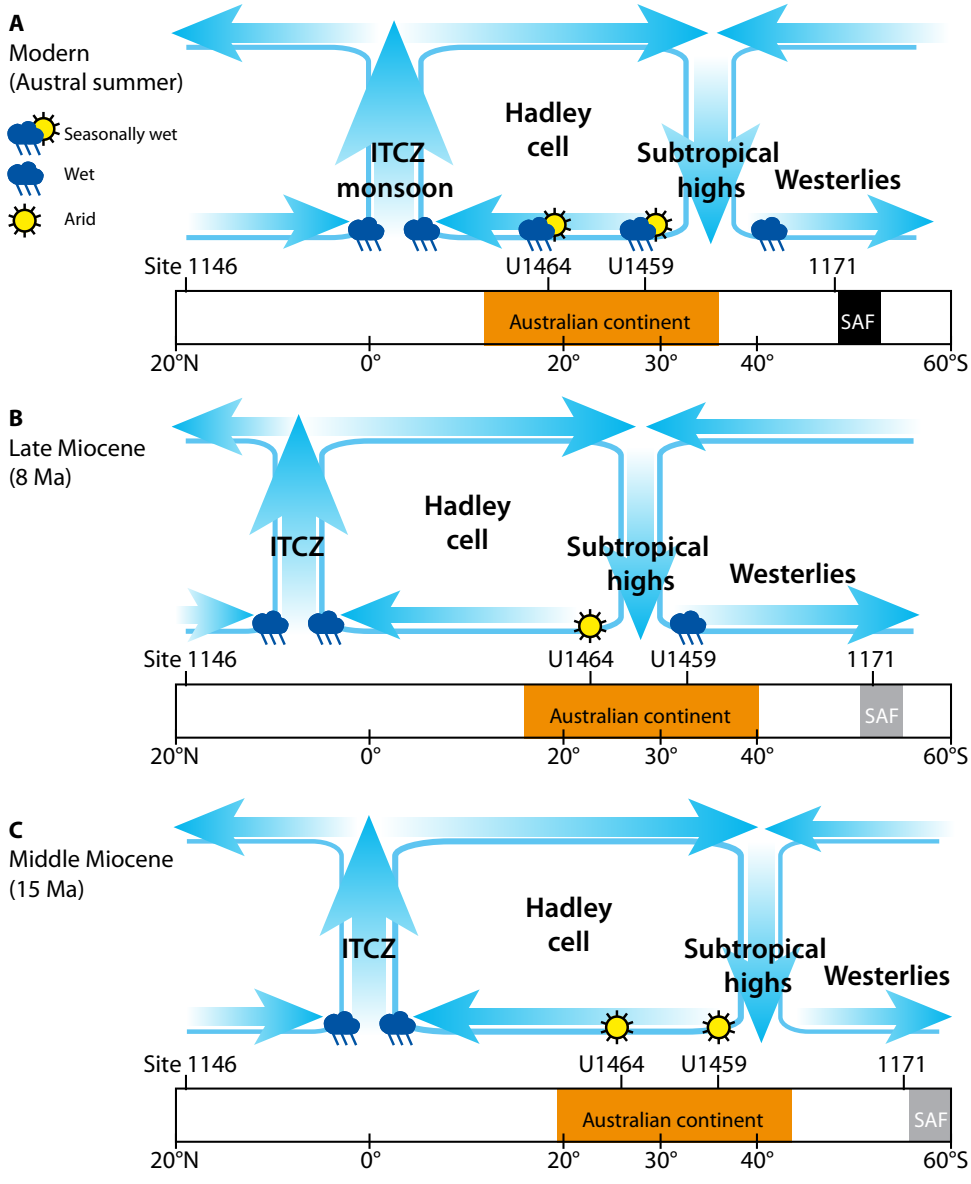

Fig. 2. Schematic meridional profiles showing relative movement of atmospheric circulation patterns. Meridional cross section from the South China Sea to Antarctica as shown in Fig. 1. The location of Australia and the drill sites are indicated at their respective paleolatitudes. Relative movement of the major climatic systems related to the Hadley circulation and oceanographic features such as the ITCZ, subtropical highs, westerlies, and Subantarctic Front (SAF) is shown for three time periods: (**A**) Modern; (**B**) Late Miocene (~8 Ma); and (**C**) Middle Miocene (~15 Ma). Cloud and sun symbols indicate wetter or drier conditions, respectively.

as arid as in the northwest (Fig. 3). This is indicated by Th/K values around 20 and very low K (%) (<0.01%) at Site U1459 from ~14 to 12 Ma, in close connection with the expansion of the Antarctic ice sheet (AIS). From 12 to 8 Ma, Th/K was consistently <10 and K values increased, pointing to progressively wetter conditions in southwest Australia (Fig. 3). After 8 Ma, conditions returned to a drier setting.

DISCUSSION

Our high-resolution records from Western Australia provide a framework to put in a global perspective. The globally warm period of the Miocene Climatic Optimum (~17 to 15 Ma) (*1*) was truncated by a major increase in ice volume on Antarctica along with a drop in global sea level at ~13.9 Ma, possibly caused by a decline in global atmospheric CO_2 (*1*, *21*) or by a switch in orbital forcing (*22*). Following the initial large increase in ice volume, the ice sheet remained relatively stable until ~8 Ma, but deep-sea temperatures continued to decrease (*1*, *23*). Continued sea surface cooling in the Southern Ocean (*25*) was accompanied by increasingly wet conditions in southwest Australia (Fig. 4), reaching a maximum at ~8 Ma. We propose a connection between cooling water masses in the Southern Ocean, an increase in sea ice cover around Antarctica, and the northward migration of the westerlies in the Late Miocene (Figs. 2 and 4). Northward migration of the westerlies may additionally also have led to a northward migration of the Hadley cell (Fig. 2). The formation of sea ice around Antarctica would have been facilitated both by an increase in the size of the

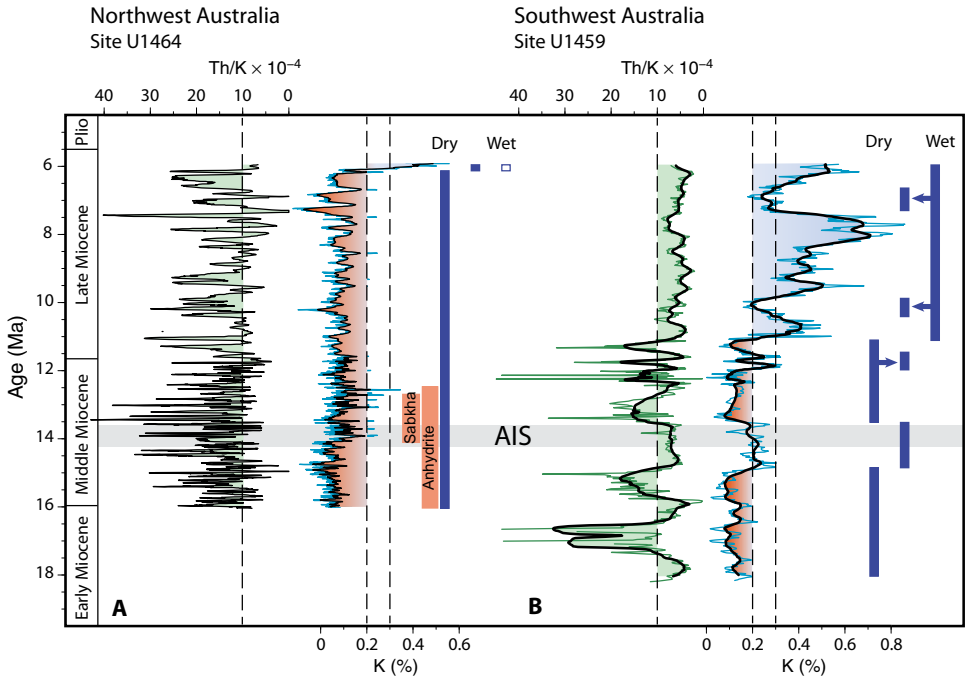

Fig. 3. Proxy data depicting 10 million year history of Middle to Late Miocene climate change in Western Australia. (**A**) Wireline log data of Th/K (green) and K (%; blue) from IODP Site U1464 (18°03.9′S, 118°37.8′E, 264-m water depth). (**B**) Wireline log data of Th/K (green) and K (%; blue) from IODP Site U1459 (28°40.2′S, 113°33.5′E, 192-m water depth). Black curves are 15-point running averages. Vertical dashed lines indicate the limits for either arid or humid intervals (see supplementary text). Vertical blue bars summarize periods of dominantly dry, intermediate, or wet conditions. Gray bar indicates the time interval of major AIS expansion.

AIS at ~13.9 Ma (*3*) and continued global oceanic cooling well into the Late Miocene (*23*, *24*). This supports the expansion of sea ice around Antarctica (*25*), leading to widespread atmospheric change in the Southern Hemisphere.

We argue that changing precipitation and river runoff reflect differences in the influence of the westerlies over southwest Australia. This implies that the northward extent of the westerlies reached 30°S to 40°S from ~12 to 8 Ma (Fig. 2). Model experiments on the Miocene glaciation (*2*, *3*) and relative seawater salinity reconstructions from the South China Sea (Fig. 4C) (*4*) suggest that both the westerlies and the ITCZ moved northward during the Late Miocene and intensified, but the timing and rate of change remained unknown until this study. Sea surface records from the Atlantic section of the Southern Ocean [Ocean Drilling Program (ODP) Site 1092] and the Tasman Rise (ODP Site 1171) show decreasing temperatures and freshening from the Middle Miocene to more glaciated conditions after expansion of the AIS (Fig. 4, B and C), interpreted as a northward movement of the Subantarctic Front (*5*, *26*). These combined observations thus support our Miocene paleoclimate inferences for southwest Australia (Fig. 2).

We provide a detailed insight into variations in the strength and latitudinal extent of the Southern Hemisphere westerlies and their influence on Australian climate during the Miocene (Fig. 2). Arid conditions in northwest Australia were similar to today and persisted for most of the Miocene, whereas southwest Australia became continuously wetter during the Late Miocene until ~8 Ma. The return to relatively arid conditions in southwest Australia after ~8 Ma is synchronous with the drying in Southeast Asia (*27*, *28*) and globally increasing dominance of grasses, which are better adapted to arid conditions (*29*). These changes could have been facilitated by a southward displacement and weakening of the Hadley cell. However, it has also been suggested that these changes were possibly related to a major uplift phase of the Himalayas (*30*) or a global decrease in atmospheric CO_2 concentrations (*21*, *25*). Our study suggests that Southern Hemispheric atmospheric circulation is highly sensitive to climate change on longer time scales. This implies that large-scale future climate change is likely to result in shifts in precipitation patterns in Australia and in large parts of Southeast Asia.

MATERIALS AND METHODS

IODP Sites U1459 (28°40.2′S, 113°33.5′E, 192-m water depth) and U1464 (18°03.9′S, 118°37.8′E, 264-m water depth) were cored in the Perth Basin and in the Roebuck Basin, respectively (Fig. 1) (*12*).

Natural gamma ray radiation downhole logging

The Hostile Environment Natural Gamma Ray Sonde (HNGS) was used on both the triple combo and Formation MicroScanner (FMS)/sonic tool strings to measure natural gamma radiation (NGR) in the formation. The HNGS uses two bismuth germanate scintillation detectors and five-window spectroscopy to determine concentrations of K (%) and Th (parts per million) from the characteristic gamma ray energies of isotopes in the ^{40}K and ^{232}Th radioactive decay series, which dominate the natural radiation spectrum. The computation of the elemental abundances uses a least-squares method to extract K and Th elemental concentrations from the spectral measurements. The HNGS filters out gamma ray energies below 500 keV, eliminating sensitivity to bentonite or KCl in the drilling mud and improving measurement accuracy. The HNGS also provides a measure of the total gamma ray emission (HSGR) and uranium-free or computed gamma ray emission (HCGR) measured in American Petroleum Institute units (gAPI). Because the HNGS response is influenced by the borehole diameter, the HNGS data were corrected for borehole diameter variations during acquisition.

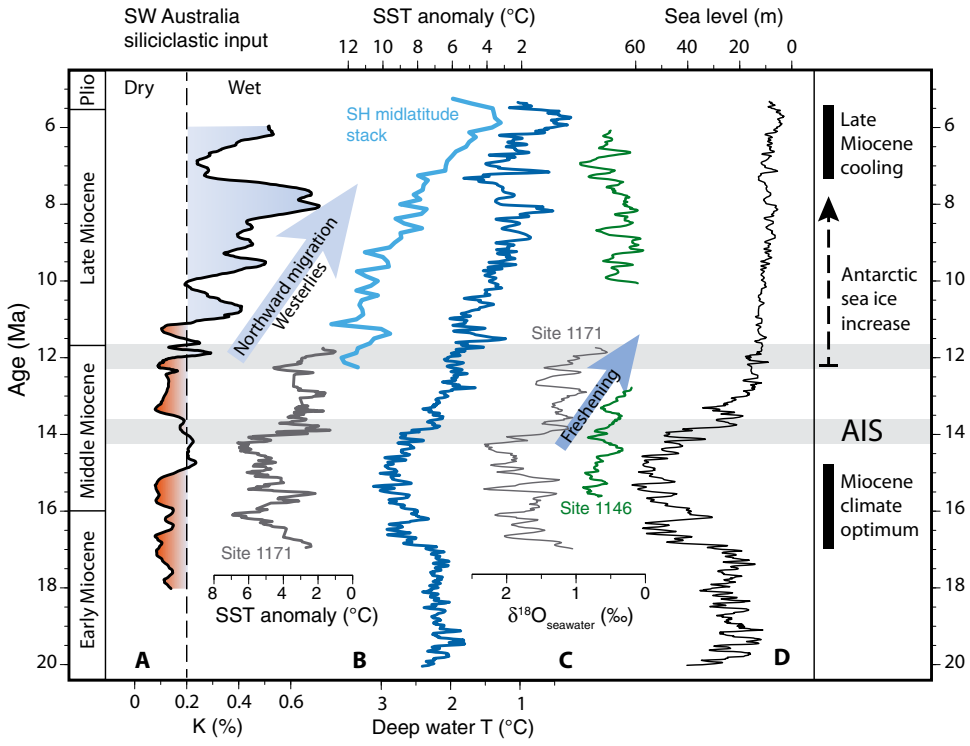

Fig. 4. Comparison of changes in southwest Australian precipitation with global climate. (**A**) Average siliciclastic input (black) as reflected by wireline log data of K (%) from IODP Site U1459 (15-point running average). Shading highlights dry (orange) versus wet (blue) conditions. (**B**) Relative changes in seawater temperature (°C) expressed as SST anomalies in the Tasman Sea (gray) relative to the Miocene minimum SSTs reconstructed at ODP Site 1171 (5-point running average) (*5*), stacked record of midlatitude Southern Hemisphere temperature anomalies (blue) relative to modern SSTs (*25*), and modeled global deep-water temperature (dark blue) based on $\delta^{18}O_{benthic}$ (50-ky running average) (*1*, *23*). (**C**) $\delta^{18}O_{seawater}$ (‰) as an indicator of relative salinity/precipitation for the Tasman Sea (gray; ODP Site 1171) (*5*) and the South China Sea (green; ODP Site 1146) (*4*, *28*). $\delta^{18}O_{seawater}$ was calculated using the $\delta^{18}O_{benthic}$ stack (*1*) as an estimate of ice volume. (**D**) Modeled sea level (m) variations (black; 50-ky running average) based on $\delta^{18}O_{benthic}$ (*1*, *23*). Gray bars indicate the time intervals of major AIS expansion and onset of hypothesized increases in Antarctic sea ice (dashed arrow).

X-ray diffraction

Eighty samples at Site U1459 were analyzed for bulk mineralogy using an x-ray diffractometer at Rutgers University (Newark, NJ, USA) (fig. S3 and table S2). The samples were oven-dried at low temperature, ground, and mounted on sample holders. The relative content of the mineral phases was obtained by x-ray diffraction using the Bruker D8 Advance Eco, with a Cu anode (1.54 Å) and LYNXEYE XE (one-dimensional mode) detector. The generator was set to 1000 W. Scans were taken at 40 kV and 25 mA, from 5° to 90° 2θ, 0.1 step size, 2 s per step, with a total time of 1754 s per sample. Bruker DIFFRAC EVA software was used for analysis after baseline removal. Peak heights and I/I corundum values from the International Centre for Diffraction Data PDF database were used to measure the relative abundance of all mineral phases.

The relative content of mineral phases in another seven bulk samples of Site U1459 was analyzed using x-ray diffraction on-board the JOIDES Resolution (fig. S2 and table S2). The bulk sediment samples were freeze-dried and grounded by hand, top-mounted onto a sample holder, and analyzed using a Bruker ASX D4 Endeavor x-ray diffractometer mounted with a VÅNTEC-1 detector using nickel-filtered CuKα radiation. All samples were scanned at 40 kV/40 mA, from 4° to 70° 2θ with a step size of 0.0087° and a speed of 0.2 s per step. The external corundum standard NIST (National Institute of Standards and Technology) 176 was measured periodically to monitor data quality. Diffractograms were evaluated using the DIFFRACplus EVA software package after baseline removal. Peak heights and I/I corundum values from the International Centre for Diffraction Data PDF database were used to measure the relative abundance of all mineral phases.

Chronology

Biostratigraphic ages are based on calcareous nannofossils (CN) and larger benthic foraminifera (LBF). Standard smear slides from core-catcher samples were analyzed at 5- to 10-m resolution at Site U1459 and 10- to 20-m resolution at Site U1464. All datum ages used here were calibrated to the most recent geological time scale (table S1) (*31*). CN were well-preserved in the Miocene strata, but their abundance was highly variable between the carbonate facies. At both sites, the Late Miocene is denoted by the presence of the marker species *Discoaster quinqueramus* (>5.59 Ma), within common (Site U1459) to very abundant (Site U1464) nannofossil assemblages. The presence of *Reticulofenestra rotaria* (>6.252 Ma; short range within biozone NN11) (*32*) further constrains a Late Miocene age at Site U1464. The older sections and shallow-marine facies were barren or only contained rare to few (<1 to 10% of sediment particles) nannofossils, but those specimens present indicate a Middle Miocene age at ~244-m core depth below sea floor (CSF-A) (Site U1459) and at ~580-m CSF-A (Site U1464).

LBF were identified visually during core description from external characteristics and, where needed, in thin sections. Their occurrences

were compared to stratigraphical zonations available for nearby areas in Indonesia (*33*–*35*) and Papua New Guinea (*36*). The occurrence of LBF was controlled by a combination of stratigraphic range (age) and paleoenvironment.

No stratigraphically important LBF were observed in the Miocene sediments of Site U1459. At Site U1464, two stratigraphically important markers were found (table S1)

1) *Flosculinella* sp. was identified in cores 356-U1464C-16R, 25R, 27R, 28R, and 32R, (442- to 595-m CSF-A). *Flosculinella* occurs in the upper part of the photic zone, including very shallow environments; its last occurrence is at 11.6 Ma (*35*, *36*).

2) *Nephrolepidina ferreroi* was recorded from 658- to 752-m CSF-A. *N. ferreroi* is a very characteristic LBF from ~16 to 11.6 Ma (Middle Miocene). It occurs in the intermediate part of the photic zone in well-ventilated environments. Its upper occurrence in U1464 was interpreted as an environmental rather than a stratigraphical event, because the very shallow environments in the younger part of the record were unsuitable for its occurrence. The lower boundary does not show such an environmental change and was interpreted as a biostratigraphical event. The first occurrence of *N. ferreroi* was dated at ~16 Ma (*34*, *37*).

The depth scale of wireline logs, wireline matched below sea floor (WMSF in meters), is different from the cored depth scale (CSF-A in meters), which is essentially meters below sea floor, along which biostratigraphic datums are reported. We converted the CSF-A depths of the biostratigraphic datums to WMSF depths by correlating distinct features in the wireline and core-based total NGR records. Subsequently, a biostratigraphic age model was constructed for the wireline records of both sites by applying linear interpolation between the biostratigraphic tie points listed in table S1.

Time series analysis and cyclostratigraphy

The wireline K-records of Sites U1459 and U1464 were converted from depth to time using the biostratigraphic age model, and then subjected to time-frequency weighted fast Fourier transform (T-F WFFT) (*38*) to detect a possible imprint of astronomical climate forcing (fig. S4). The biostratigraphic age model for Site U1459 estimates sedimentation rates accurately between 12 and 5 Ma because spectral amplitude is high at frequencies close to the expected frequencies of eccentricity [100 and 405 thousand years (ky) periodicity] (fig. S4). In the older part of the Site U1459, K-record high spectral amplitude was observed at periodicities higher than the expected 405-ky period of the Earth's eccentricity. This suggests that the eccentricity cycles have been significantly "stretched" in the time domain by the biostratigraphic age model. This was caused by assigning a maximal age of 22.82 Ma to the bottom of the record, which may actually have a younger age, based on the sole presence of *Reticulofenestra haqii*, a nannofossil species that was common throughout the Miocene since its first occurrence in biozone NN2 (*32*). To better constrain the Site U1459 age model in the older portion of the record, we applied a cyclostratigraphic approach. We used a 300- to 500-ky band-pass filter in the upper half of the record and a very wide band-pass filter (500 to 1000 ky; fig. S4) in the older part of the record. We chose such a large filter to extract variations in the K-record that are related to 405-ky eccentricity, but were stretched in the biostratigraphic age model. The band-pass–filtered signal was then correlated to the La2011 eccentricity solution (*39*). In the younger part of the record, this correlation was straightforward because the biostratigraphic age model in that interval is well constrained. Between 12 and 5 Ma, extremes in the low-pass–filtered signal from Site U1459 were separated by only a few tens of thousands of years from extremes in the 405-ky component of La2011. In other words, the tuning process did not significantly alter the initial age model for 12 to 5 Ma. In the older portion of the record, the same approach of correlating extremes between the filtered signal and the eccentricity solution was maintained. Here, we compressed the Site U1459 record until the low-frequency variations in the K-record matched the 405-ky cycles in La2011. This tuning process brings the oldest part of the record from 22.82 Ma in the biostratigraphic age model to ~18 Ma (fig. S4).

The evolutive harmonic analysis of the Site U1464 K-record showed highs in spectral amplitude concentrated around the expected frequency of the 100-ky eccentricity cycles. This observation suggested that the biostratigraphic age model for Site U1464 gives an accurate estimate of sedimentation rates throughout the Miocene interval at this site. For Site U1464, we applied the same cyclostratigraphic approach as for the upper half of U1459. Aware of the fact that the Miocene interval at this site consists of shallow marine and, possibly, subaerial deposits, we applied this approach. Hence, the sequence is likely to have numerous interruptions in sedimentation, which imply important pitfalls for a cyclostratigraphic approach. Nevertheless, the impact of these interruptions seems relatively limited on the long-term (>100 ky) eccentricity cycles (figs. S4 and S5).

In fig. S5, we show the T-F WFFT spectra for the astronomically calibrated K-records for Sites U1459 and U1464 (window size, 600 ky). We find increased spectral power in the 100-ky eccentricity band from 11.5 to 10 Ma at both sites. This corresponds to a period of high-amplitude 100-ky eccentricity cycles in the La2011 astronomical solution (*39*), as illustrated by the T-F WFFT of a normalized eccentricity-tilt-precession (ETP) composite in fig. S5. This imprint of high-amplitude 100-ky variation in the eccentricity of Earth's orbit has also been observed in benthic $\delta^{18}O$ isotope records from the South China Sea (ODP Site 1146) (*40*) and the Southwest African continental margin (ODP Site 1085) (indicated by orange rectangles on fig. S5) (*41*). The latter two studies also reported two instances of strong obliquity imprint around 9.5 and 12 Ma, in response to relatively strong obliquity forcing (indicated by red arrows on fig. S5) (*42*). At Site U1464, the T-F WFFT exhibits increased spectral power at a frequency of 0.02 cycles/ky at ~12 Ma. We tentatively interpreted this increased spectral power as an obliquity signal, in agreement with the astronomical pattern found in the benthic $\delta^{18}O$ records from Sites 1146 and 1085. Unfortunately, the temporal resolution of the K-records from the upper half of Sites U1464 and U1459 is too low to evaluate a possible obliquity imprint.

SUPPLEMENTARY MATERIALS

Supplementary material for this article is available at http://advances.sciencemag.org/cgi/content/full/3/5/e1602567/DC1

Expedition 356 Scientists

Supplementary Text

fig. S1. Lithostratigraphic column for IODP Site U1464, including recovery, biostratigraphic tie points, interpreted facies, K (%), Th/K versus sediment depth, and photos of sabhka and dolostone facies.

fig. S2. Lithostratigraphic column for IODP Site U1459 including recovery, biostratigraphic tie points, K (%), and Th/K versus sediment depth.

fig. S3. Correlation of the K-record with K-feldspar obtained from bulk mineralogy XRD analyses plotted versus depth, and as scatter plot.

fig. S4. T-F WFFT of the K-records from sites U1459 and U1464 along their respective biostratigraphic age model, and age versus sediment depth.

fig. S5. T-F WFFT of the K-records from Sites U1459 and U1464 versus ETP solution (*39*, *42*), and in comparison with those performed on the benthic $\delta^{18}O$ records from ODP Site 1146 in the South China Sea (*40*) and ODP Site 1085 in the South Atlantic (*41*) for the same time interval.

table S1. Biostratigraphic datums used for the biostratigraphic age model.
table S2. Paired potassium feldspar (%), quartz (%, only shipboard; n.d., no data), and K-log (%) results versus depth in core for Site U1459.
References (*43*–*48*)

REFERENCES AND NOTES

1. J. C. Zachos, G. R. Dickens, R. E. Zeebe, An early Cenozoic perspective on greenhouse warming and carbon-cycle dynamics. *Nature* **451**, 279–283 (2008).
2. H. Ao, A. P. Roberts, M. J. Dekkers, X. Liu, E. J. Rohling, Z. Shi, Z. An, X. Zhao, Late Miocene–Pliocene Asian monsoon intensification linked to Antarctic ice-sheet growth. *Earth Planet. Sci. Lett.* **444**, 75–87 (2016).
3. R. DeConto, D. Pollard, D. Harwood, Sea ice feedback and Cenozoic evolution of Antarctic climate and ice sheets. *Paleoceanography* **22**, PA3214 (2007).
4. A. Holbourn, W. Kuhnt, M. Regenberg, M. Schulz, A. Mix, N. Andersen, Does Antarctic glaciation force migration of the tropical rain belt? *Geology* **38**, 783–786 (2010).
5. A. E. Shevenell, J. P. Kennett, D. W. Lea, Middle Miocene Southern Ocean cooling and Antarctic cryosphere expansion. *Science* **305**, 1766–1770 (2004).
6. G. J. Marshall, Trends in the Southern Annular Mode from observations and reanalyses. *J. Climate* **16**, 4134–4143 (2003).
7. B. A. Raut, C. Jakob, M. J. Reeder, Rainfall changes over southwestern Australia and their relationship to the Southern Annular Mode and ENSO. *J. Climate* **27**, 5801–5814 (2014).
8. T. Fan, C. Deser, D. P. Schneider, Recent Antarctic sea ice trends in the context of Southern Ocean surface climate variations since 1950. *Geophys. Res. Lett.* **41**, 2419–2426 (2014).
9. T. Schneider, T. Bischoff, G. H. Haug, Migrations and dynamics of the intertropical convergence zone. *Nature* **513**, 45–53 (2014).
10. J. C. H. Chiang, C. M. Bitz, Influence of high latitude ice cover on the marine Intertropical Convergence Zone. *Clim. Dynam.* **25**, 477–496 (2005).
11. J. R. Toggweiler, D. W. Lea, Temperature differences between the hemispheres and ice age climate variability. *Paleoceanography* **25**, PA2212 (2010).
12. S. J. Gallagher, C. S. Fulthorpe, K. A. Bogus, Reefs, oceans, and climate: A 5 million year history of the Indonesian throughflow, Australian monsoon, and subsidence on the northwest shelf of Australia. *Int. Ocean Discovery Program. Sci. Prospectus* **356**, 10.14379/iodp.sp.356.2014 (2014).
13. R. D. Müller, M. Sdrolias, C. Gain, B. Steinberger, C. Heine, Long-term sea-level fluctuations driven by ocean basin dynamics. *Science* **319**, 1357–1362 (2008).
14. S. E. Calvert, T. F. Pedersen. "Elemental proxies for palaeoclimatic and palaeoceanographic variability in marine sediments: Interpretation and application" in *Proxies in Late Cenozoic Paleoceanography*, C. Hillaire-Marcel, A. De Vernal, Eds. (Elsevier, 2007), pp. 567–644.
15. W. Kuhnt, A. Holbourn, J. Xu, B. Opdyke, P. De Deckker, U. Röhl, M. Mudelsee, Southern Hemisphere control on Australian monsoon variability during the late deglaciation and Holocene. *Nat. Commun.* **6**, 5916 (2015).
16. J.-B. W. Stuut, F. Temmesfeld, P. A. De Deckker, A 550 ka record of aeolian activity near North West Cape, Australia: Inferences from grain-size distributions and bulk chemistry of SE Indian Ocean deep-sea sediments. *Quat. Sci. Rev.* **83**, 83–94 (2014).
17. K. H. Morgan, Development, sedimentation and economic potential of palaeoriver systems of the Yilgarn Craton of Western Australia. *Sediment. Geol.* **85**, 637–656 (1993).
18. H. A. Martin, Cenozoic climatic change and the development of the arid vegetation in Australia. *J. Arid Environ.* **66**, 533–563 (2006).
19. N. Herold, M. Huber, D. R. Greenwood, R. D. Müller, M. Seton, Early to Middle Miocene monsoon climate in Australia. *Geology* **39**, 3–6 (2011).
20. C. A. Metzger, G. J. Retallack, Paleosol record of Neogene climate change in the Australian outback. *Austr. J. Earth Sci.* **57**, 871–885 (2010).
21. Y. G. Zhang, M. Pagani, Z. Liu, S. M. Bohaty, R. DeConto, A 40-million-year history of atmospheric CO_2. *Philos. Trans. R. Soc. A* **371**, 20130096 (2013).
22. A. Holbourn, W. Kuhnt, M. Schulz, H. Erlenkeuser, Impacts of orbital forcing and atmospheric carbon dioxide on Miocene ice-sheet expansion. *Nature* **438**, 483–487 (1995).
23. B. De Boer, R.S.W. van de Wal, L.J. Lourens, R. Bintanja, Transient nature of the Earth's climate and the implications for the interpretation of benthic $\delta^{18}O$ records. *Palaeogeogr. Palaeoclimatol. Palaeoecol.* **335–336**, 4–11 (2012).
24. T. D. Herbert, K. T. Lawrence, A. Tzanova, L. Cleaveland Peterson, R. Caballero-Gill, C. S. Kelly, Late Miocene global cooling and the rise of modern ecosystems. *Nat. Geosci.* **9**, 843–847 (2016).
25. R. Gersonde, B. Censarek, Middle-late Southern Ocean climate development and its implication on Antarctic ice sheet development - Diatom evidence from Atlantic sector ODP Sites. *Geophys. Res. Abstr.* **8**, 06285 (2006).
26. H. Kuhnert, T. Bickert, H. Paulsen, Southern Ocean frontal system changes precede Antarctic ice sheet growth during the middle Miocene. *Earth Planet. Sci. Lett.* **284**, 630–638 (2009).
27. A. Zhisheng, J. E. Kutzbach, W. L. Prell, S. C. Porter, Evolution of Asian monsoons and phased uplift of the Himalaya-Tibetan plateau since late Miocene times. *Nature* **411**, 62–66 (2001).
28. S. Steinke, J. Groeneveld, H. Johnstone, R. Rendle-Bühring, East Asian summer monsoon weakening after 7.5 Ma: Evidence from combined planktonic foraminifera Mg/Ca and $\delta^{18}O$ (ODP Site 1146; northern South China Sea). *Palaeogeogr. Palaeoclimatol. Palaeoecol.* **289**, 33–43 (2010).
29. E. J. Edwards, C. P. Osborne, C. A. E. Strömberg, S. A. Smith; C_4 Grasses Consortium, The origins of C_4 grasslands: Integrating evolutionary and ecosystem science. *Science* **328**, 587–591 (2010).
30. P. D. Clift, K. V. Hodges, D. Heslop, R. Hannigan, H. Van Long, G. Calves, Correlation of Himalayan exhumation rates and Asian monsoon intensity. *Nat. Geosci.* **1**, 875–880 (2008).
31. F. Gradstein, J. Ogg, M. Schmitz, G. Ogg, *The Geologic Time Scale 2012* (Elsevier, 2012).
32. J. R. Young, "Neogene" in *Calcareous Nannofossil Biostratigraphy*, P. Bown, Ed. 225–265 (Springer, 1998).
33. P. Lunt, T. Allan, *Larger foraminifera in Indonesian biostratigraphy, calibrated to isotopic dating*: Geological Research Development Centre (GRDC) Museum, Bandung, Indonesia, Workshop on Micropaleontology, (2004), 109pp.
34. W. Renema, Fauna Development of Larger Benthic Foraminifera in the Cenozoic of Southeast Asia, in *Biogeography, Time and Place: Distributions, Barriers and Islands*, W. Renema, Ed. (Springer, 2007), pp. 179–215.
35. W. Renema, V. Warter, V. Novak, J. R. Young, N. Marshall, F. Hasibuan, Age of Miocene fossil localities in the Northern Kutai Basin (East Kalimantan, Indonesia). *Palaios* **30**, 26–39 (2015).
36. T. L. Allan, J. A. Trotter, D. J. Whitford, M. J. A. Korsch, "A correlation of Sr isotope stratigraphy and foraminiferal biostratigraphy in tertiary limestones of Papua New Guinea" (INIS, Research Report 1995–2000, 2000). https://inis.iaea.org/search/search.aspx?orig_q=RN:32042814
37. N. Marshall, V. Novak, I. Cibaj, W. Krijgsman, W. Renema, J. Young, N. Fraser, A. Limbong, R. Morley, Dating Borneo's deltaic deluge: Middle Miocene progradation of the Mahakam Delta. *Palaios* **30**, 7–25 (2015).
38. M. Martinez, J.-F. Deconinck, P. Pellenard, L. Riquier, M. Company, S. Reboulet, M. Moiroud, Astrochronology of the Valanginian–Hauterivian stages (Early Cretaceous): Chronological relationships between the Paraná–Etendeka large igneous province and the Weissert and the Faraoni events. *Global Planet. Change* **131**, 158–173 (2015).
39. J. Laskar, A. Fienga, M. Gastineau, H. Manche, La2010: A new orbital solution for the long-term motion of the Earth. *Astron. Astrophys.* **532**, A89 (2011).
40. A. Holbourn, W. Kuhnt, S. Clemens, W. Prell, N. Andersen, Middle to late Miocene stepwise climate cooling: Evidence from a high-resolution deep water isotope curve spanning 8 million years. *Paleoceanography* **28**, 688–699 (2013).
41. T. Westerhold, T. Bickert, U. Röhl, Middle to late Miocene oxygen isotope stratigraphy of ODP Site 1085 (SE Atlantic): New constrains on Miocene climate variability and sea-level fluctuations. *Palaeogeogr. Palaeoclimatol. Palaeoecol.* **217**, 205–222 (2005).
42. J. Laskar, P. Robutel, F. Joutel, M. Gastineau, A. C. M. Correia, B. Levrard, A long-term numerical solution for the insolation quantities of the Earth. *Astron. Astrophys.* **428**, 261–285 (2004).
43. M. Zabel, R. R. Schneider, T. Wagner, A. T. Adegbie, U. de Vries, S. Kolonic, Late Quaternary climate changes in Central Africa as inferred from terrigenous input to the Niger Fan. *Quat. Res.* **56**, 207–217 (2001).
44. K. M. Yarincik, R. W. Murray, L. C. Peterson, Climatically sensitive eolian and hemipelagic deposition in the Cariaco Basin. Venezuela, over the past 578,000 years: Results from Al/Ti and K/Al. *Paleoceanography* **15**, 210–228 (2000).
45. D. Šimíček, O. Bábek, Spectral gamma-ray logging of the Gres d'Annot, SE France: An outcrop analogue to geophysical facies mapping and well-log correlation sand-rich turbidite reservoirs. *Mar. Petrol. Geol.* **60**, 1–17 (2015).
46. S. N. Ehrenberg, T. A. Svånå, Use of spectral gamma-ray signature to interpret stratigraphic surfaces in carbonate strata: An example from the Finnmark carbonate platform (Carboniferous-Permian), Barents Sea. *AAPG Bull.* **85**, 295–308 (2001).
47. J. H. Doveton, Lithofacies and geochemical facies profiles from nuclear wire-line logs: New subsurface templates for sedimentary modeling. *Bull. - Kans. Geol. Surv.* **233**, 101–110 (1991).
48. S. P. Hesselbo, Spectral gamma-ray logs in relation to clay mineralogy and sequence stratigraphy, Cenozoic of the Atlantic margin, offshore New Jersey, in *Proceedings of the Ocean Drilling Program, Scientific Results*, **150**, (1996), pp. 411–422.

Acknowledgments: This research used samples and data provided by the IODP. We thank the JRSO (JOIDES Resolution Science Operator) staff and the Siem Offshore crew for their invaluable assistance and skill during the expedition. We acknowledge the Expedition 356 drilling proposal proponents. We thank two anonymous reviewers for their constructive comments. We are grateful to S. Mustaque from Queens College and M. Ramlogan, A. Rouff, and E. Elzinga from Rutgers University (Newark, NJ, USA) for the use of the Bruker D8

Advanced XRD supported by NSF-EAR-1337450. **Funding:** We thank the German Research Council (grant GR 3528/3-1; to J.G.); the Swedish Research Council (VR grants 2011-4866 and 2016-04434; to J.H.); the ARC Basin GENESIS Hub (to S.J.G.); the Australian Research Council and the ANZIC office (HVM, Expedition 356 Scientists group); the US Science Support Program (to C.M.M., Expedition 356 Scientists group); and the Ministry of Oceans and Fisheries, Korea (EYL). **Author contributions:** J.G. developed the concepts and wrote the manuscript together with J.H. and W.R. C.M.M., D.D.V., B.A.C., C.S.F., and K.B. contributed to the data analysis and discussions concerning the writing and interpretation. J.H., J.G., C.M.M., and D.D.V. drafted the figures. All coauthors were participants on the IODP Expedition 356 and participated in generating the data published herein, the data analysis, and shipboard interpretations, and contributed to the writing of this manuscript. **Competing interests:** The authors declare that they have no competing interests. **Data and materials availability:** Shipboard Expedition 356 data will be publicly available from 27 February 2017 and can be accessed at http://web.iodp.tamu.edu/LORE/. Additional data related to this paper may be requested from the authors.

Submitted 18 October 2016
Accepted 9 March 2017
Published 10 May 2017
10.1126/sciadv.1602567

Citation: J. Groeneveld, J. Henderiks, W. Renema, C. M. McHugh, D. De Vleeschouwer, B. A. Christensen, C. S. Fulthorpe, L. Reuning, S. J. Gallagher, K. Bogus, G. Auer, T. Ishiwa, Expedition 356 Scientists, Australian shelf sediments reveal shifts in Miocene Southern Hemisphere westerlies. *Sci. Adv.* **3**, e1602567 (2017).

ScienceAdvances

Australian shelf sediments reveal shifts in Miocene Southern Hemisphere westerlies

Jeroen Groeneveld, Jorijntje Henderiks, Willem Renema, Cecilia M. McHugh, David De Vleeschouwer, Beth A. Christensen, Craig S. Fulthorpe, Lars Reuning, Stephen J. Gallagher, Kara Bogus, Gerald Auer, Takeshige Ishiwa and Expedition 356 Scientists

Sci Adv **3** (5), e1602567.
DOI: 10.1126/sciadv.1602567